Conf-820896--7

CONF-820896--7

Nordic Meeting, August 16-20, 1982 DE83 015716

Heavy-Ion Reaction Mechanisms Studied with the Spin Spectrometer

M. L. Halbert
Oak Ridge National Laboratory*, Oak Ridge, Tennessee 37830

Nordic Meeting, August 16-20, 1982

Heavy-Ion Reaction Mechanisms Studied with the Spin Spectrometer

M. L. Halbert
Oak Ridge National Laboratory*, Oak Ridge, Tennessee 37830

Experimental data and statistical-model calculations for xn and αxn products of the reaction $^{20}Ne + ^{146}Nd$ at 136 MeV are shown to be in generally good agreement, indicating that equilibrium processes are dominant. Preliminary results on the heavy-ion ejectiles from $^{19}F + ^{159}Tb$ are presented.

I. The Angular-Momentum Dimension

In many heavy ion reactions most of the initial-system orbital angular momentum is ultimately carried away by γ rays. If the product nuclei are rotational, the γ rays are primarily stretched E2. In such cases a measurement of the γ-ray multiplicity, M_γ, can provide a good estimate of the angular momentum of the entry state, that is, the state of the product nucleus after all particle emissions have occurred. Since the angular momentum removed by particles often can be adequately estimated with the help of some model, we are able to infer what regions of entrance-channel ℓ space lead to various reaction products. One might say that this opens a new dimension in nuclear reaction studies. Formerly one had to integrate over the angular momentum variable. Now it is available for learning more about the reaction mechanism.

The usefulness of M_γ measurements for heavy-ion reactions was first demonstrated about 10 years ago at the Niels Bohr Institute [1]. Since then

a number of laboratories have used γ-multiplicity arrays. These arrays have generally been rather small and able to register only a small sample of the γ radiation emitted in any single event. Such experiments usually produced statistically reliable information on the average M_γ, somewhat less accurate data on the width of the M_γ distribution, and (in favorable cases) some idea of its skewness. Not much information on the total γ-ray energy could be obtained because so many of the γ rays escaped.

With the development of sum spectrometers, again pioneered at the Niels Bohr Institute [2], better data on the total energy emitted as γ rays was obtained. This information is valuable because it tells us the excitation energy, E^*, of the entry state.

A new generation now exists of 4π γ-ray detector systems approaching the ideal of registering all the γ rays accompanying a single nuclear collision. Such systems can provide, for each event, M_γ and E^* at the same time. They also provide angular correlations, continuum γ-ray spectra, energy-energy correlations, and timing information. The first of these new devices, the Spin Spectrometer [3] at Oak Ridge National Laboratory, consists of 72 NaI detectors forming an almost spherical shell ~ 18 cm thick around the target. Some of the experiments we have done with this instrument were aimed primarily at getting new information on heavy-ion reaction mechanisms and they are the subject of this paper. Our recent results on nuclear structure at very high spin are covered in Dr. Jääskeläinen's contribution.

The work I will report on is a collaborative effort between Oak Ridge National Laboratory (J. R. Beene, G. R. Young, R. L. Ferguson,

J. H. Barker [4], and D. C. Hensley) and Washington University in St. Louis (D. G. Sarantites, M. Jääskeläinen [5], F. A. Dilmanian, H. Puchta [6], and R. Woodward).

II. Complete Fusion and Equilibrium Decay

For the first experiment with the Spin Spectrometer [7], we wanted to choose a system that would show no significant nonequilibrium phenomena. We knew from previous work [8] that there is no evidence of nonequilibrium neutron emission in bombardments of ^{150}Nd with ^{20}Ne up to 175 MeV. In this first experiment we bombarded a ^{146}Nd target with 136-MeV ^{20}Ne. We substituted a Ge counter for one of the NaI detectors in the Ball and recorded data from all the detectors whenever the Ge counter was triggered. The purpose of the Ge was to enable us to identify particular reaction channels by means of the γ-ray lines known in the various possible reaction products.

Figure 1(a) shows a density distribution of all the events in coincidence with the $2^+ \rightarrow 0^+$ transition of ^{160}Yb, the residual nucleus after evaporation of 6 neutrons. The abscissa k is the number of NaI detectors that registered γ rays and the ordinate H is the sum of the NaI pulse heights for that event. The next step is a transformation from the (H,k) map to an (E^*,M_γ) map. This is based on measurements of the response of each detector to γ-ray lines of five different energies and in effect corrects for scattering from one detector to another, coincidence summing, and escape of some radiation from the Ball. The results of this

transformation are shown by the contour maps in Fig. 1(b) for the principal xn products, namely ^{161}Yb, ^{160}Yb and ^{159}Yb. The dot marks the peak of each mountain. The contours are all referred to the 6n peak, and represent factors of $\sqrt{2}$, 2, 4, and 8. In Fig. 2(a) and (b) we show projections of these distributions on the M_γ and E^* axes for each channel.

We thus have very complete information on the population of the entry states and are in a position to test the predictions of the statistical model in a very detailed way. We use a computer program that is a modification of JULIAN-PACE, the Monte Carlo code of Hillman and Eyal with additions by Gavron [9]. The results shown here are for a level density parameter of a = A/9.5; as will be pointed out below, other values can be used. We chose to represent the entrance-channel ℓ distribution by $\sigma_\ell = \pi\lambda^2(2\ell+1)\ [1 + \exp(\ell-\ell_{fus})/d]^{-1}$ with $\ell_{fus} = 59.5$ and d = 1. These parameters closely approximate the distribution predicted by the sum rule model of Wilczynski et al. [10]. This ℓ distribution is shown by the solid line in Fig. 2(f); the dotted line is for d = 5. Note that after the particles are evaporated, the resulting entry-state J distributions [Fig.2(f)] are not as sharp edged and their shape is less sensitive to d.

Figure 1(c) shows the calculated entry-state distribution in (E^*,J) space for d=1. We want to compare with the experimental results which are in (E^*,M_γ) space. We can easily do this by continuing the Monte Carlo process, keeping track of how these entry states decay by γ emission. It was here, in the γ decay region, that our modifications

of JULIAN-PACE are of the most importance. We replaced the energy-independent E1 γ-ray strength by one that includes the giant dipole resonance. Its position and width were taken from experimental systematics [11] with a strength given by the energy-weighted sum rule. We used the so-called Lorentzian shape, a sum of two Breit-Wigner terms [12] for positive and negative resonance energies. Statistical E2 and M1 transitions with constant strengths of 1.0 W.u. and 0.005 W.u., respectively, were included together with collective stretched E2 transition with B(E2) = 100 W.u. for E_γ below 2 MeV. This means that the γ cascades proceed mainly by E1 transitions to the vicinity of the yrast line and then by stretched E2 transitions to the ground state for even-even products or to an yrast state with $J < 2$ for odd-A products. The yrast lines were taken from the rotating liquid drop model [13] above spin 22. Below 22 the moment of inertia was assumed to decrease linearly with decreasing J to approximate the behavior typical of rotational nuclei.

In Fig. 2(c) and (d) we show the calculated M_γ and E^* distributions. For the odd-A products, where not all of the angular momentum is carried off by observable E2 γ rays, we have shifted the calculated M_γ distributions by 2.2 units, based on the known decay scheme of ^{161}Yb [14]. The agreement with experiment is generally quite good both in shape and absolute magnitudes and is not sensitive to the choice of parameters. Very similar results can be obtained with the level density parameter varied from A/10.5 to A/7.5 provided that small adjustments are made either in the position of the yrast line (but not its slope, i.e., we don't vary the moment of inertia) or in the E1 γ-ray strength (from

1.0 to 1.8 times the energy-weighted sum rule). The calculations for the αxn channels also show good agreement with the data.

The relationship between the entrance-channel ℓ distribution and the resulting M_γ distribution is likewise insensitive to these variations of parameters, so we feel that we can safely deduce some features of the ℓ distributions from our M_γ data. In Fig. 2(e) we compare the sum of the xn and αxn channels for experiment (dots) and theory (lines) for two choices of the diffuseness parameter d, d = .1 and d = 5. The biggest difference is in the slope of the upper edge. It is clear that the smaller value agrees better with the data. We can say definitely that $d < 2$. The position of the edge is given quite well by the choice $\ell_{fus} = 59.5$.

We now compare the experimental and calculated 2-parameter (E^*, M_γ) distributions in Fig. 1(b) and (d). In general the agreement is good, giving additional confidence that this reaction goes predominantly through equilibrated states. A couple of discrepancies may be noted, however. First, the predicted maximum of the 7n product doesn't agree with the observed value. We don't regard this as a serious problem because the spectroscopy of this product nucleus, ^{159}Yb, is partially unknown and consequently we don't know exactly how to relate J to M_γ. This could lead to a shift of several units in M_γ. Second, the widths of the distributions perpendicular to the yrast line are about 30% narrower in the calculation than in the experiment. This discrepancy does not depend on the choice of parameters provided that they preserve a reasonable agreement between the theoretical and experimental projections.

Changing the width of the giant resonance leaves this discrepancy about the same. Thus at present we are not sure what this phenomenon is trying to tell us.

Figure 3 shows the entry lines (average excitation energy at each M_γ) for the 5n, 6n, and 7n channels. The lines are from the calculations, while the experimental data are shown by the points. The agreement is excellent except for the very highest multiplicities. We believe this is a manifestation of a change in nuclear structure at high spin which is the subject of Dr. Jääskeläinen's contribution.

We conclude that the fusion of 136-MeV ^{20}Ne with ^{146}Nd gives products that decay predominantly by an equilibrium process, and that the statistical model can be used to supply the experimentally unknown angular-momentum information on the evaporated particles. Combining such calculations with the experimental data from the γ decay we can now provide a rather complete picture of the angular-momentum dependence of this type of reaction.

III. Nonequilibrium Processes

In another experiment with the Spin Spectrometer we chose to emphasize the noncompound features. We bombarded ^{159}Tb with 180-MeV ^{19}F (9.5 MeV/A). Eleven counter telescopes were installed inside the Spin Spectrometer at angles from 15° to 150°. These were all silicon surface-barrier (ΔE,E) telescopes. Whenever any of the E counters was triggered we recorded the pulse heights and times of the particles and all the information from the NaI crystals. There were in addition 2 single Si

detectors at 8° to the beam intended for detection of heavy evaporation residues. This has been our most complicated experiment so far. There were altogether 26 silicon counters in addition to the 70 NaI detectors in the Ball. Each could give a pulse height and a time signal, for a total of over 190 possible signals to be processed.

All of the telescopes recorded α particles and protons. Four of them, the ones at 20°, 30°, 40°, and 50°, also provided data on heavy ions from Li through Mg.

The analysis of this experiment is far from complete. We have made more progress on the heavy ions and I will present preliminary results for them. The first step is to determine, if possible, the process by which the heavy ions were produced. Thinking first of binary reactions, that is, final states consisting of only two particles, there are two limiting pictures to consider. In one of these, the observed heavy ion is little more than a spectator. It splits off from the projectile at an early stage of the interaction with the target nucleus, traveling with approximately the beam velocity and direction, while the remainder of the projectile fuses with the target. The process known variously as incomplete fusion [15-18], massive transfer [19], or breakup fusion [20] is conceived of in this way. In work we did several years ago with a small γ-multiplicity array, we found that $\langle M_\gamma \rangle$ for the partially fused system varies linearly with the captured mass [17]. This suggests that the angular momentum carried away by the escaping particle is proportional to its mass, which is what one would expect classically if the breakup always occurs at a well-localized distance, say at the nuclear

surface. The energy of these particles is given approximately by the optimum Q value for the particle transfer [10], which corresponds to the conservation of linear and angular momentum along classical trajectories for the entrance and exit channels.

The other limiting case is that of deep inelastic or damped collisions. These are collisions in which the projectile and the target remain in contact for an extended time while their relative kinetic energy is converted to rotational energy and heat. If the damping is complete, the particles separate with zero relative energy and appear in the final system with energy due only to their Coulomb repulsion. One expects to see such fully damped products well beyond the grazing angle, which in this case is about 30°. In this process the angular momentum deposited in the heavy fragment is generally larger than in the beam-velocity case.

These two extreme cases should be distinguishable on the basis of particle energy and angular momentum in the heavy fragment. We can show this nicely with contour maps of the experimental data on particle energy, E, vs. coincidence fold, k. Figure 4 is such a plot for ^{15}N particles at 40°. The axis labels apply to the small picture at the bottom. The upper picture is an expanded view of the same data. The particle energy corresponding to the optimum Q value and to the fully damped situation are marked by arrows. Within each group there is some variation of k with particle energy: there are fewer γ rays emitted when the particle takes away more energy. Figure 5 shows the isotopes of nitrogen at 30°. The damped component is very weak or absent.

There are additional particle groups. In the 30° ^{14}N and ^{15}N maps (Fig. 5), we can see a beam-velocity or Q_{opt} group that has very low k, i.e., very few γ rays. For this group the heavy partner is being left in a low-lying state. A possible mechanism for this would be a projectile breakup, not followed by fusion, which leads to a three-body final state with very little energy transferred to the target. The escaping particle has already left the vicinity and so its energy is not affected by the subsequent fusion or lack of fusion. We have seen this sort of thing before. In an experiment done several years ago with an ^{16}O beam and a Ge(Li) detector, we saw events in which only very low-lying states of the target nucleus were observed in coincidence with ^{12}C fragments [21]. The group of particles with low energy and low k, seen for example in Fig. 4, is probably due to reactions with target impurities such as carbon and oxygen.

By placing a mask on the desired group of particles in these maps, we have obtained (H,k) maps for the beam-velocity component alone and for the damped component alone. From these we have obtained average values of H and k. Then, from the so called reverse responses based on the measured response functions of the NaI [3], we have deduced average values of M_γ and E^* for each particle group at each angle. Figure 6 shows the average multiplicity for all the particles at 20° and 30°. The value of M_γ goes down with increasing mass, an effect we should expect if the escaping fragment really carries off angular momentum according to its mass.

We can show the mass dependence in another way. Figure 7 shows the same $\langle M_\gamma \rangle$ data plotted as a function of the mass captured from the

projectile. The overall trend given by the straight line is interesting. In the time-honored approximate relation between $\langle M_\gamma \rangle$ and J, we expect $\langle M_\gamma \rangle - 3$ or 4 to be equal to half the average angular momentum of the entry states. On the average each captured nucleon is bringing in 2 x 0.95 = 1.9 $\hbar$ to the fused system. Suppose complete fusion occurs. In this case the average angular momentum would be 19 times 1.9 = 36 $\hbar$; this is in reasonable agreement with the prediction 41 from the sum-rule model. However, this cannot be the whole story. The mass dependence shown by the isotopes of one element is not the same as the overall effect given by the straight line; their slopes are clearly quite different. Note also that there is a jump of an additional unit of multiplicity, that is, about 2 units of spin, when Z changes by one unit. This may be related to the matching of the Coulomb orbits in the initial and final systems.

We have done a series of calculations using the sum-rule model [10] as input for the statistical model. The ℓ distributions predicted by the sum-rule model were converted to spin distributions on the assumption that the non-fusing part of the projectile carries off a fraction of the initial angular momentum equal to the ratio of escaping mass to projectile mass. The resulting spin distributions were then the input for the modified version of JULIAN-PACE. The predicted γ-ray multiplicities for a number of channels are shown in Fig. 6. The predictions follow the general trend of the data quite well. However, they are too high by ~ 30%. Either the escaping particle carries off more angular momentum than we assumed or somehow not all of the remaining angular momentum is

being transferred into the product of the partial fusion. Another possible explanation is that in many cases the particle we observe is not the primary ejectile, but a secondary resulting from decay of the primary. Such a process will always move us toward lower multiplicity because $\langle M_\gamma \rangle$ is lower for the heavier primary. We hope to determine the relative number of these events by investigating particle-particle coincidences.

The $\langle M_\gamma \rangle$ data for the damped component at 40° is shown in Fig. 8; $\langle M_\gamma \rangle$ varies only slightly with ejectile. The sticking-model predictions for several choices of angular momentum are also shown. As has been observed in several other experiments, the lighter fragments show a smaller transfer of angular momentum than the grazing value. From the incomplete-fusion point of view, the grazing ℓ is not the most reasonable choice here. If instead we use for each channel the average angular momentum given by the sum-rule model, we get the intermediate points which come much closer to the experimental data. In fact, they bridge the gap between the grazing ℓ value, which applies to fragments similar to the projectile, and the critical ℓ value for complete fusion, the limit we approach at the left.

So in broad outline it seems sensible to make use of the sum-rule model when we need information on the angular momenta of the escaping particles. And in a practical sense I don't know of any other choice at present.

We can give also some preliminary information on the second moments of the multiplicity distribution. We show in Fig. 9 the relative standard deviation of the k distributions at all four angles. These are not

equal to the relative widths in M_γ, but they ought to give us some idea of what those widths are. The results show relative widths from 25 to 40%, increasing at first with mass of the ejectile. The predictions are from the statistical model with input spin distributions from the sum-rule model and have the instrumental resolution [3] folded in. The experimental spin distributions are considerably wider than the model predicts. This could be another indication of ejectile breakup. For example, suppose some of the C we observe consists of secondaries from breakup of N and O ejectiles. Since these heavier particles arise from lower ℓ values than do the primary carbon ions, we would expect a large relative standard deviation in M_γ. Of course, another possibility is that the assumptions of the sum-rule model that lead to very narrow ℓ distributions may not be sufficiently realistic.

Since we have the average excitation energy $\langle E^* \rangle$ as well as $\langle M_\gamma \rangle$, we easily obtain the average γ-ray energy, $\langle E_\gamma \rangle$ (Fig. 10). For 20° and 30°, the values are between about 1.0 and 1.5 MeV with a trend toward higher energy for the heavier ejectiles. The statistical model predicts a constant value of just under 1 MeV for the γ rays from the partially fused system. If the ejectile is excited, the γ rays it emits will most likely be of higher energy and will tend to increase the measured $\langle E_\gamma \rangle$ above this calculated value. At 40° the damped and beam-velocity components are both about 1.2 MeV, independent of the ejectile. These observations will require more study than we've had time to give them so far. I should mention that $\langle M_\gamma \rangle \sim 3.5$ and $\langle E_\gamma \rangle \sim 1.8$ MeV for the low-k, low-particle-energy component on the (E,k) maps. One would expect

reactions with light nuclei such as C or O to give such results. This supports our decision to exclude these groups from our analyses.

We now discuss the cross sections. Figure 11 shows the angular distributions for each Z. The damped and the beam-velocity components have been used, but the low-E group has been omitted. Note that data for Li, Be, and B recorded by the telescopes at 15°, 25°, and 60° have been included. Near 25° the curves for the heavier ions are drawn to match for Li, Be, and B. These results are similar to data from other experiments, in particular, for the KVI results from 10-MeV/A ^{14}N on the same target [10].

To obtain total cross sections we need to integrate over angles. The results depend somewhat, perhaps at the 20% level, on how the extrapolation to small angles is made. Lacking any further information we have simply used the average slope of the Li, Be, and B data for the heavier products.

The isotopic yields are very similar at 20° and 30°, as Fig. 12 shows. Since 20° and 30° contribute the most to the integral, we have used these data to separate the cross sections according to isotopes. Figure 13 shows the isotopic cross sections in comparison with the predictions of the sum-rule model. The points are the experiment, the bars the model. For ^{15}N, $^{16,17,18}O$, and ^{18}F, it is clear that the experimental yield is much larger than the predictions. We should remember here that this model involves touching of the nuclear matter distribution and thus will not include few-nucleon transfers that occur in the nuclear halo. For many of the channels that are especially strong, the structure

of the ejectile is related simply to that of the ^{19}F projectile, for example, $^{11}B = {}^{19}F - 2\alpha$. Figure 14 is another representation of the same data, namely the ratio of the experimental value to the prediction. On the whole, the agreement is reasonable: nearly all of the ratios are within a factor of two of unity. However, we must keep in mind that the experimental values here are uncertain because of the extrapolations and approximations that had to be made. And there is always the question of how significant are the secondaries.

In conclusion, I should emphasize the preliminary nature of the results in this section. It was with some reluctance that I have submitted this report, particularly as my co-workers have had no chance to review it. I hope that the data are interesting enough to compensate for the incompleteness of the analysis.

References

*Operated by Union Carbide Corporation under contract W-7405-eng-26 with the U.S. Department of Energy.

1. Hagemann, G. B., Broda, R., Herskind, B., Ishihara, M., Ogaza, S., and Ryde, H., Nucl. Phys. A245, 166 (1975).
2. Tjøm, P. O., Espe, I., Hagemann, G. B., Herskind, B., and Hillis, D. L., Phys. Lett. 72B, 439 (1978).
3. Jääskeläinen, M., Sarantites, D. G., Woodward, R., Dilmanian, F. A., Hood, J. T., Jääskeläinen, R., Hensley, D. C., Halbert, M. L., and Barker, J. H., Nucl. Instrum. Methods (in press).
4. Present address: South Carolina Electric & Gas Company, P.O. Box 764, Columbia, SC 29218.
5. Present address: Department of Physics, University of Jyväskylä, Jyväskylä, Finland.
6. Present address: Sektion Physick, Universität München, 8046 Garching, West Germany.
7. Sarantites, D. G., Jääskeläinen, M., Woodward, R., Dilmanian, F. A., Hensley, D. C., Barker, J. H., Beene, J. R., Halbert, M. L., and Milner, W. T., Phys. Lett. (in press).
8. Westerberg, L., Sarantites, D. G., Hensley, D. C., Dayras, R. A., Halbert, M. L., and Barker, J. H., Phys. Rev. C 18, 796 (1979).
9. Gavron, A., Phys. Rev. C 21, 230 (1980).
10. Wilczynski, J., Siwek-Wilczynska, K., van Driel, J., Gonggrijp, S., Hageman, D. C. J. M., Janssens, R. V. F., Lukasiak, J., Siemssen, R. H., and van der Werf, S. Y., Nucl. Phys. A373, 109 (1982).

11. Hanna, S. S., in Giant Multipole Resonances, (ed. F. Bertrand), Table I, Harwood, New York, 1980.

12. Bohr, A., and Mottelson, B., Nuclear Structure, Vol. II, p. 477, Benjamin, Reading, Mass., 1975.

13. Cohen, S., Plasil, F., and Swiatecki, W. J., Ann. Phys. (N.Y.) 82, 567 (1974).

14. Riedinger, L. L., Nucl. Phys. A347, 141 (1980) and private communication.

15. Inamura, T., Ishihara, M., Fukuda, T., Shimoda, T., and Hiruta, H., Phys. Lett. 68B, 51 (1977).

16. Siwek-Wilczynska, K., van Voorthuysen, E. H. du Marchie, van Popta, J., Siemssen, R. H., and Wilcynski, J., Nucl. Phys. A330, 150 (1979).

17. Geoffroy, K. A., Sarantites, D. G., Halbert, M. L., Hensley, D. C., Dayras, R. A., and Barker, J. H., Phys. Rev. Lett. 43, 1303 (1979).

18. Barker, J. H., Beene, J. R., Halbert, M. L., Hensley, D. C., Jääskeläinen, M., Sarantites, D. G. and Woodward, R., Phys. Rev. Lett. 45, 424 (1980).

19. Zolnowski, D. R., Yamada, H., Cala, S. E., Kahler, A. C., and Sugihara, T. T., Phys. Rev. Lett. 41, 92 (1978); Yamada, H., Zolnowski, D. R., Cala, S. E., Kahler, A. C., Pierce, J., and Sugihara, T. T., Phys. Rev. Lett. 43, 605 (1979).

20. Udagawa, T., and Tamura, T., Phys. Rev. Lett. 45, 1331 (1980).

21. Novotny, R., analysis based on data from Ref. 18 (private communication).

Figure Captions

FIG. 1. Entry-state distributions for xn products from 136-MeV ^{20}Ne on ^{146}Nd. (a) Experimental density map in (H,k) space for the 6n channel. (b) Contour maps of experimental results in (E^*,M_γ) space for the strongest xn channels. (c) Contour maps of calculated results in (E^*,J) space from the statistical model. (d) Contour map of results in (E^*,M_γ) space from the same calculations as in (c). The cross-section contours in (b), (c) and (d) decrease going outward by the factors of 1.4, 2.0, 4.0, and 8.0 relative to the peak value of the 6n channel and are represented by the dotted, full, dashed and dash-dotted curves, respectively. The heavy dots locate the maximum intensity for each channel. The ^{160}Yb yrast line used in the calculations is shown by the curve below the contours.

FIG. 2. Projections of entry-state distributions. (a) Experimental cross sections of the xn channels as a function of M_γ. (b) Experimental cross sections of the xn channels as a function of E^*. (c) Calculated cross sections of the xn channels as a function of M_γ. (d) Calculated cross sections of the xn channels as a function of E^*. The calculations are based on an entrance-channel ℓ distribution with $\ell_{fus} = 59.5$ and a diffuseness $d = 1$. (e) Experimental cross sections (points) and calculated J distributions (lines) for the sum of the xn and αxn channels as a function of M_γ. (f) Calculated entrance-channel ℓ distributions and the resulting J distributions summed over all xn and αxn channels. The calculated results in (e) and (f) are for $d = 1$ (solid lines) and $d = 5$ (dashed lines).

FIG. 3. Entry lines for the principal xn channels. The points represent experimental results (Δ = 5n, $\square$ = 6n, $\bigcirc$ = 7n) while the lines are the results of statistical-model calculations. The lowest curve is the yrast line used in the calculations.

FIG. 4. Density map for 40-degree ^{15}N from 180-MeV ^{19}F on ^{159}Tb as a function of particle energy, E, and γ-ray coincidence fold, k. The axis labels refer to the lower distribution. The upper distribution is an expansion of part of the lower one.

FIG. 5. Density map for isotopes of N at 30°.

FIG. 6. Average γ-ray multiplicity of heavy ions from 180-MeV ^{19}F on ^{159}Tb at 20° (•) and 30° (o). The results of statistical model calculations using the sum-rule model for the entrance-channel ℓ distributions are shown by the triangles.

FIG. 7. Average γ-ray multiplicity at 20° and 30° as a function of mass transferred from the projectile to the target, A_t. The line drawn through the points may be represented by $2(\langle M_\gamma \rangle - 3.4) = 1.9\ A_t$.

FIG. 8. Average γ-ray multiplicity of the damped component of heavy ions at 40° (•). The other points represent sticking model calculations for various choices of initial average angular momentum.

FIG. 9. Relative standard deviation of k for the beam-velocity component at four angles. The calculated results based on statistical-model calculations with initial J distributions from the sum-rule model are also shown (x).

FIG. 10. Average γ-ray energy at four angles. BVC: beam-velocity component. DC: damped component.

FIG. 11. Angular distributions of heavy ions from 180-MeV ^{19}F on ^{159}Tb.

FIG. 12. Isotopic fractions of heavy ions emitted at 20° and 30°.

FIG. 13. Integrated cross sections for heavy ions from 180-MeV ^{19}F on ^{159}Tb (dots) compared with predictions of the sum-rule model for $T = 3.5$ MeV and $\Delta = 1.7$ (histogram).

FIG. 14. Ratios of experimental integrated cross sections to sum-rule predictions for 180-MeV ^{19}F on ^{159}Tb.

ORNL-DWG 82-11691

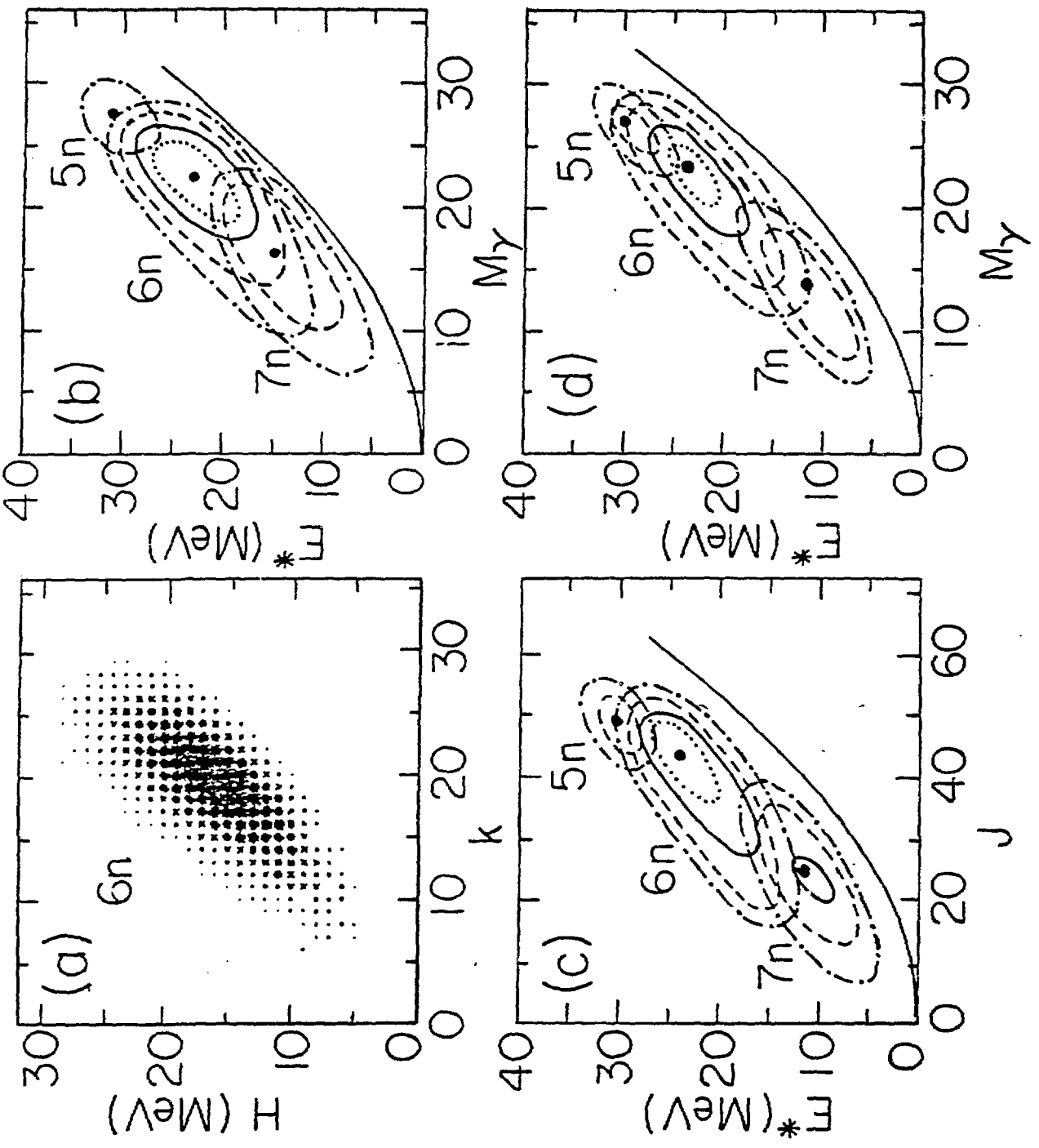

Fig. 1

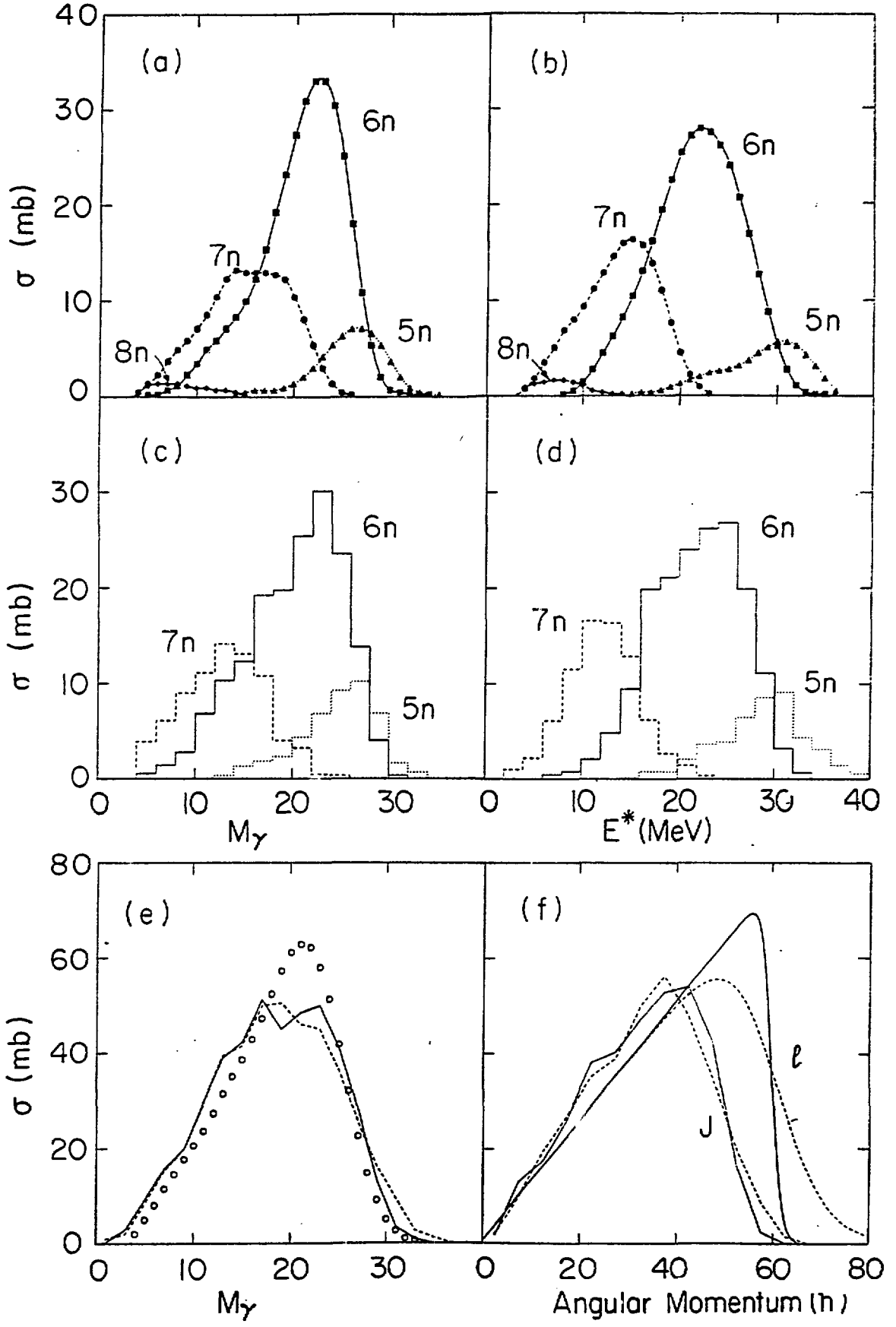

Fig. 2

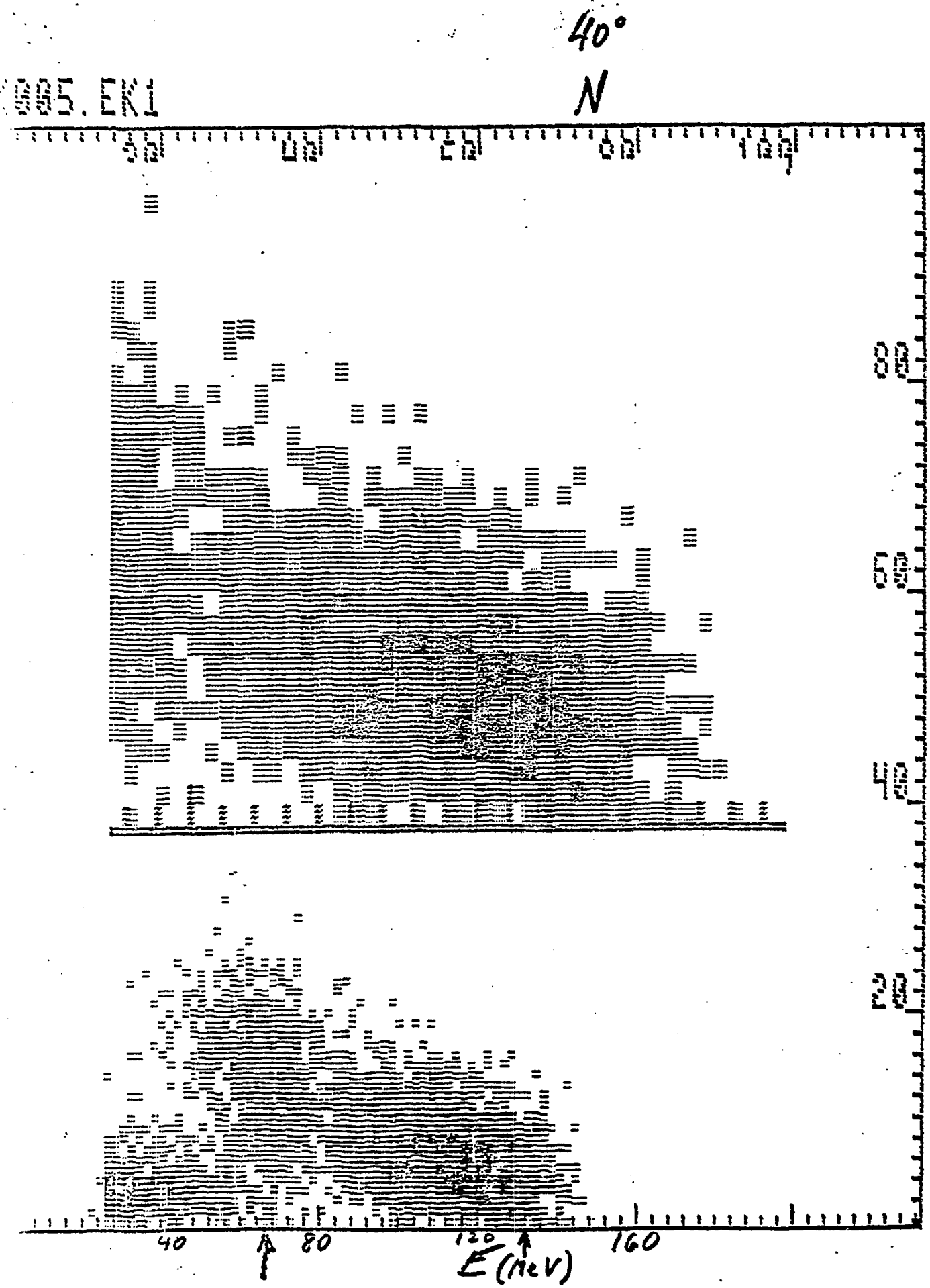

Fig. 4

Fig. 5

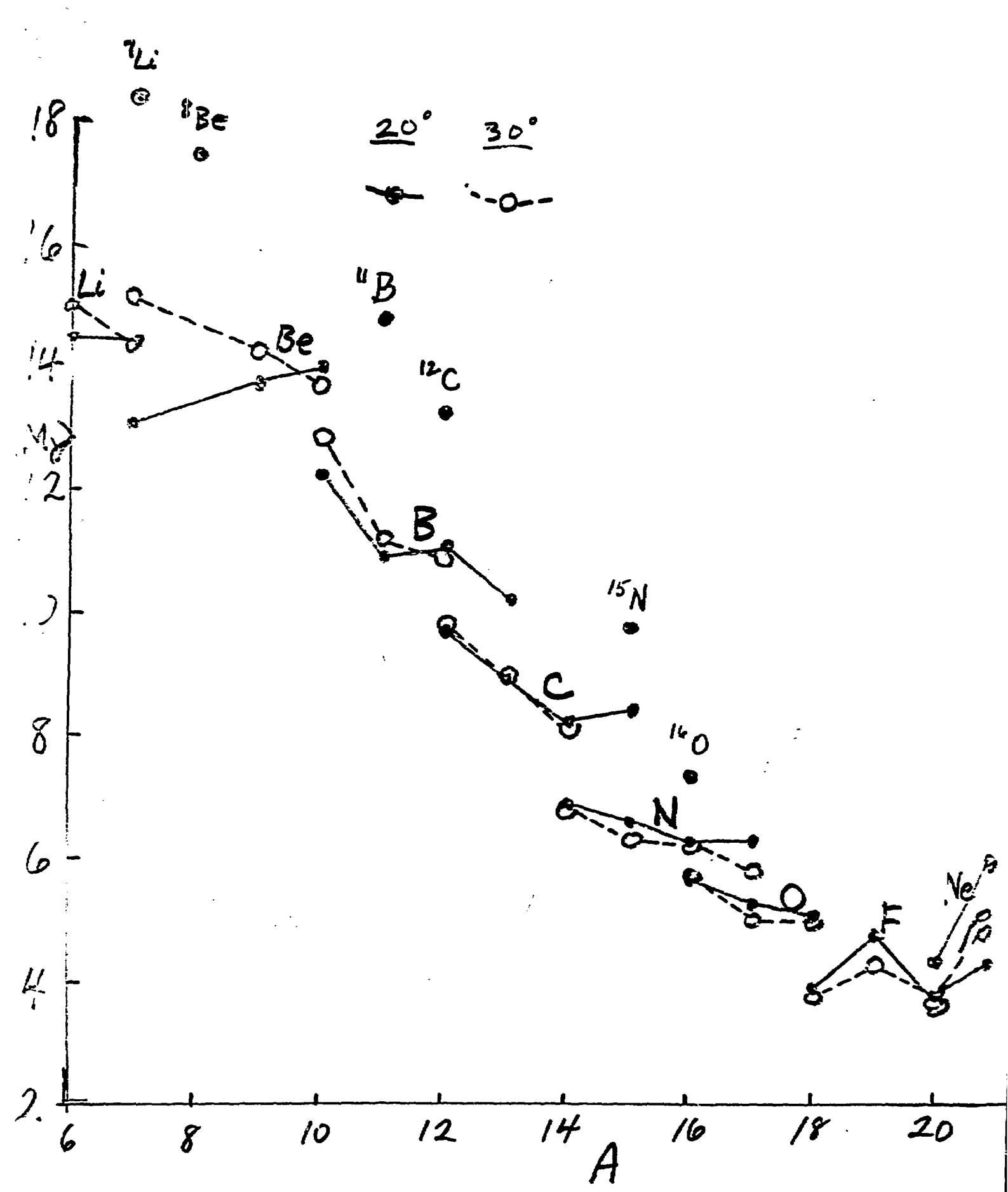
7Li
8Be
20°
30°
11B
12C
15N
16O
Li
Be
B
C
N
O
F
Ne
18
16
14
12
8
6
4
2
6
8
10
12
14
16
18
20
A

Fig. 6

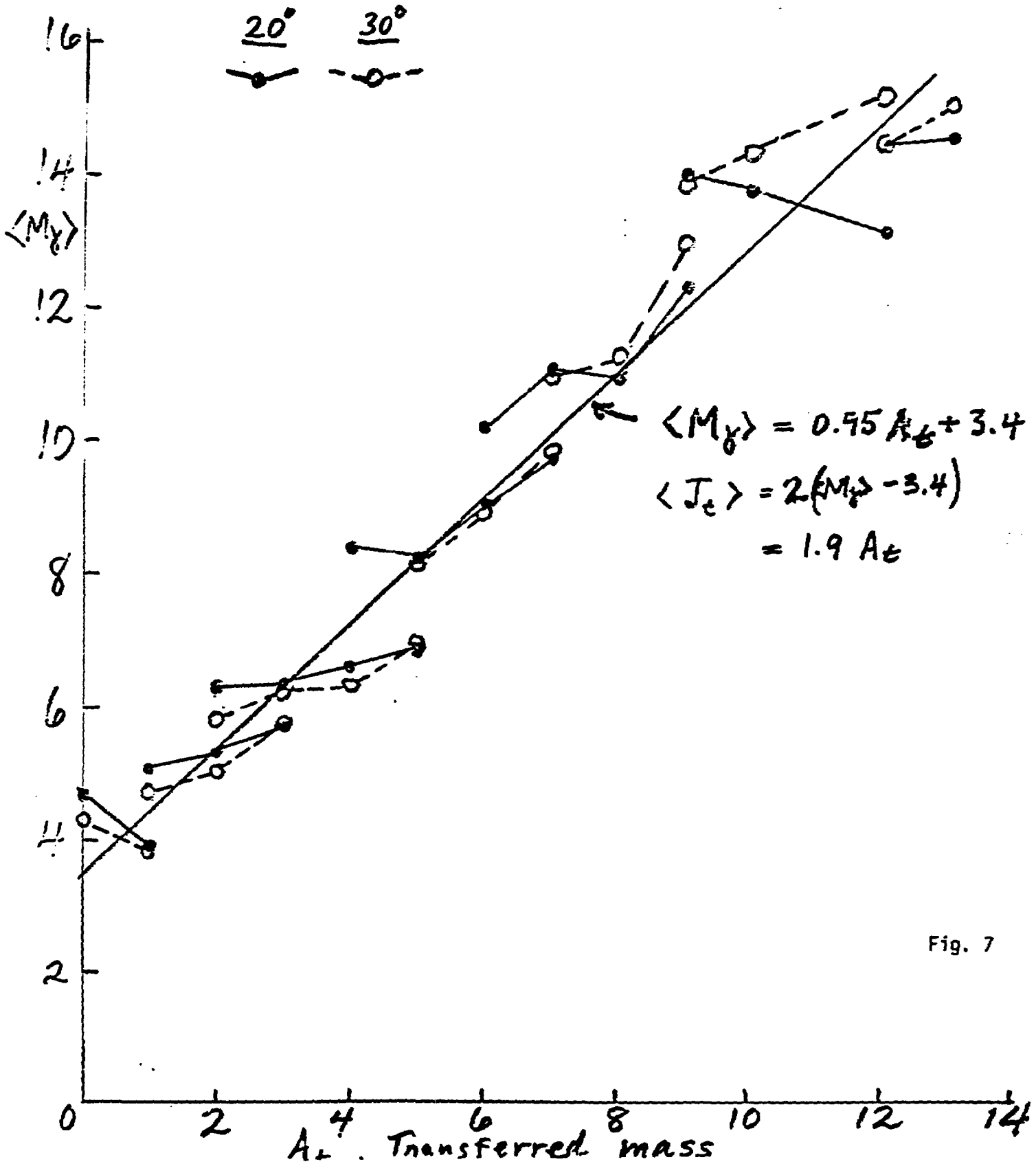
20°
30°
16
14
12
10
8
6
4
2
0
2
4
6
8
10
12
14
⟨Mγ⟩
$\langle M_\gamma \rangle = 0.95 A_t + 3.4$
$\langle J_t \rangle = 2(\langle M_\gamma \rangle - 3.4)$
$= 1.9 A_t$
A_t. Transferred mass

Fig. 7

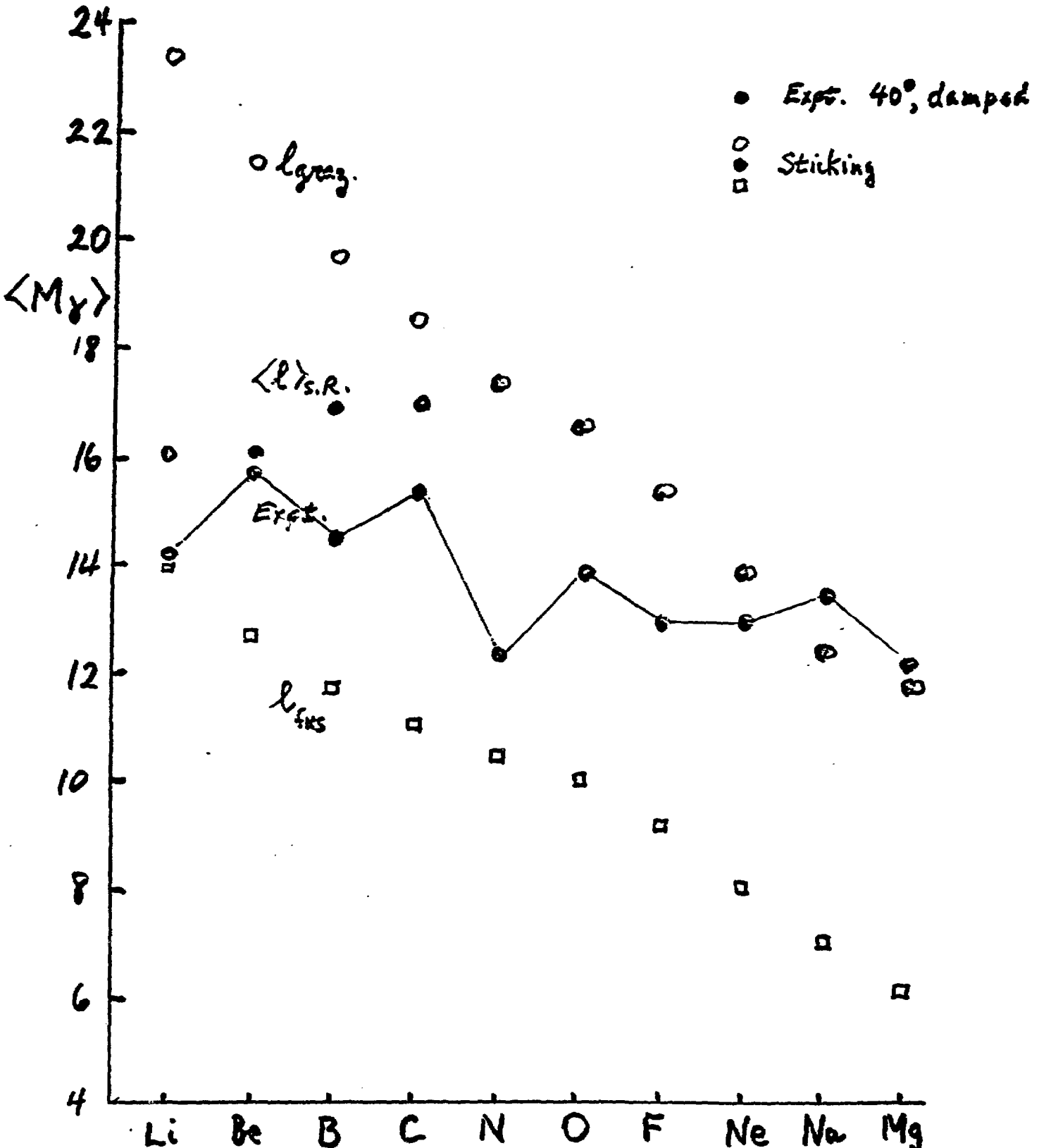
24
22
20
18
16
14
12
10
8
6
4
$\langle M_\gamma \rangle$
$l_{grazg.}$
$\langle l \rangle_{s.R.}$
Expt.
l_{fus}
Expt. 40°, damped
Sticking
Li
Be
B
C
N
O
F
Ne
Na
Mg

Fig. 8·

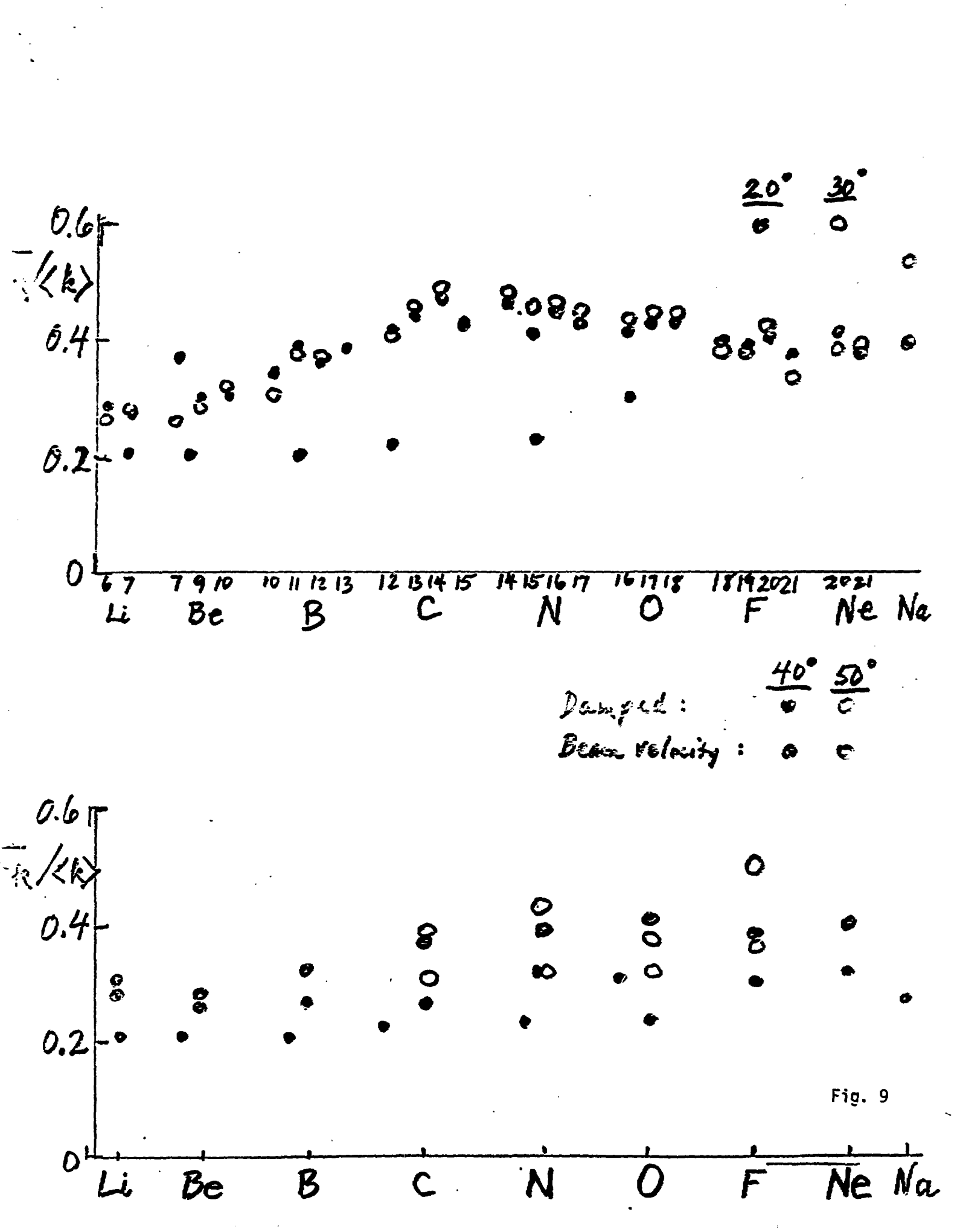
20°
30°
0.6
$\bar{R}/\langle k \rangle$
0.4
0.2
0
6 7 7 9 10 10 11 12 13 12 13 14 15 14 15 16 17 16 17 18 18 19 20 21 20 21
Li Be B C N O F Ne Na
40°
50°
Damped :
Beam velocity :
0.6
$\bar{R}/\langle k \rangle$
0.4
0.2
0
Li Be B C N O F Ne Na

Fig. 9

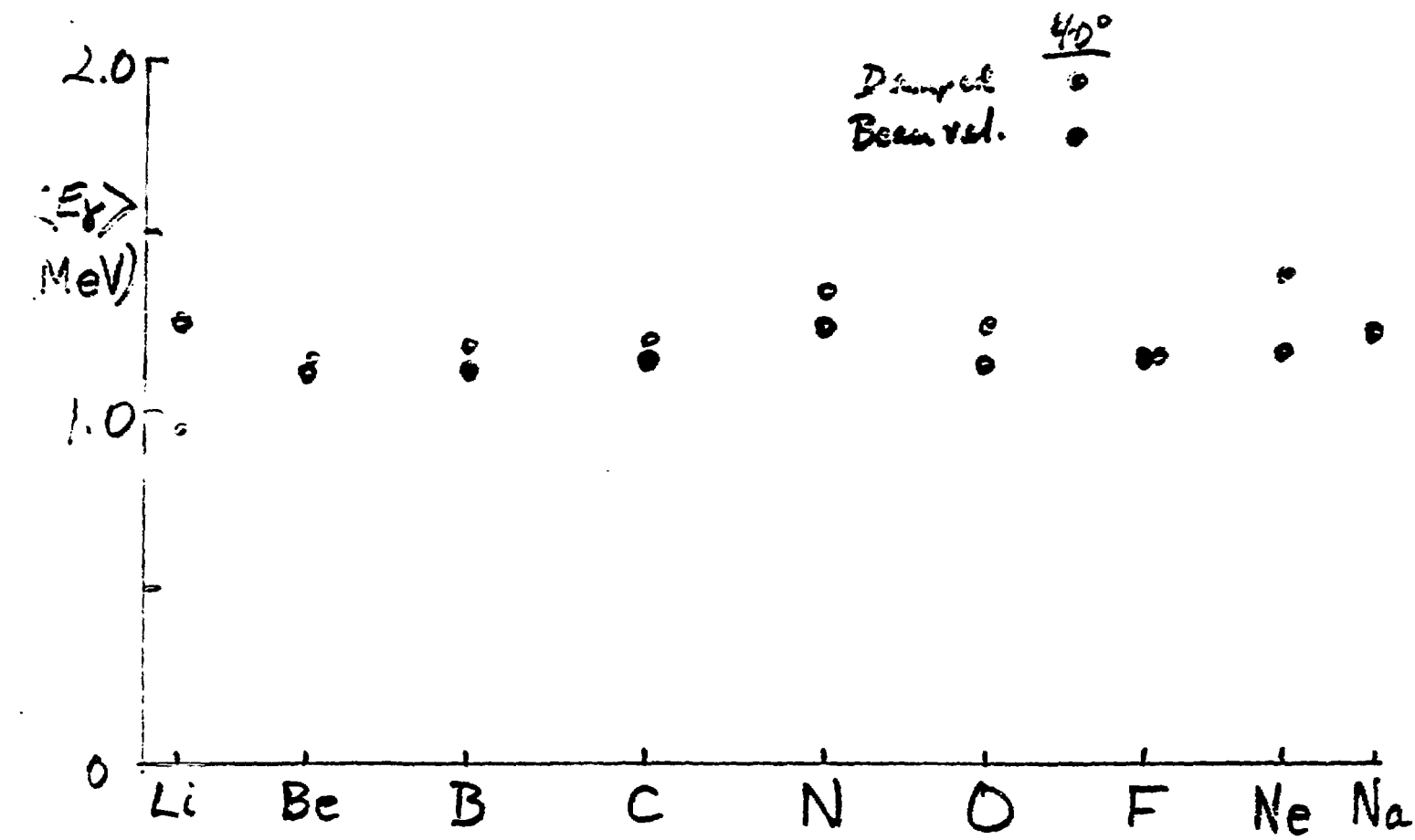
40°
Beam vel.
2.0
⟨Eγ⟩
MeV)
1.0
0
Li
Be
B
C
N
O
F
Ne
Na

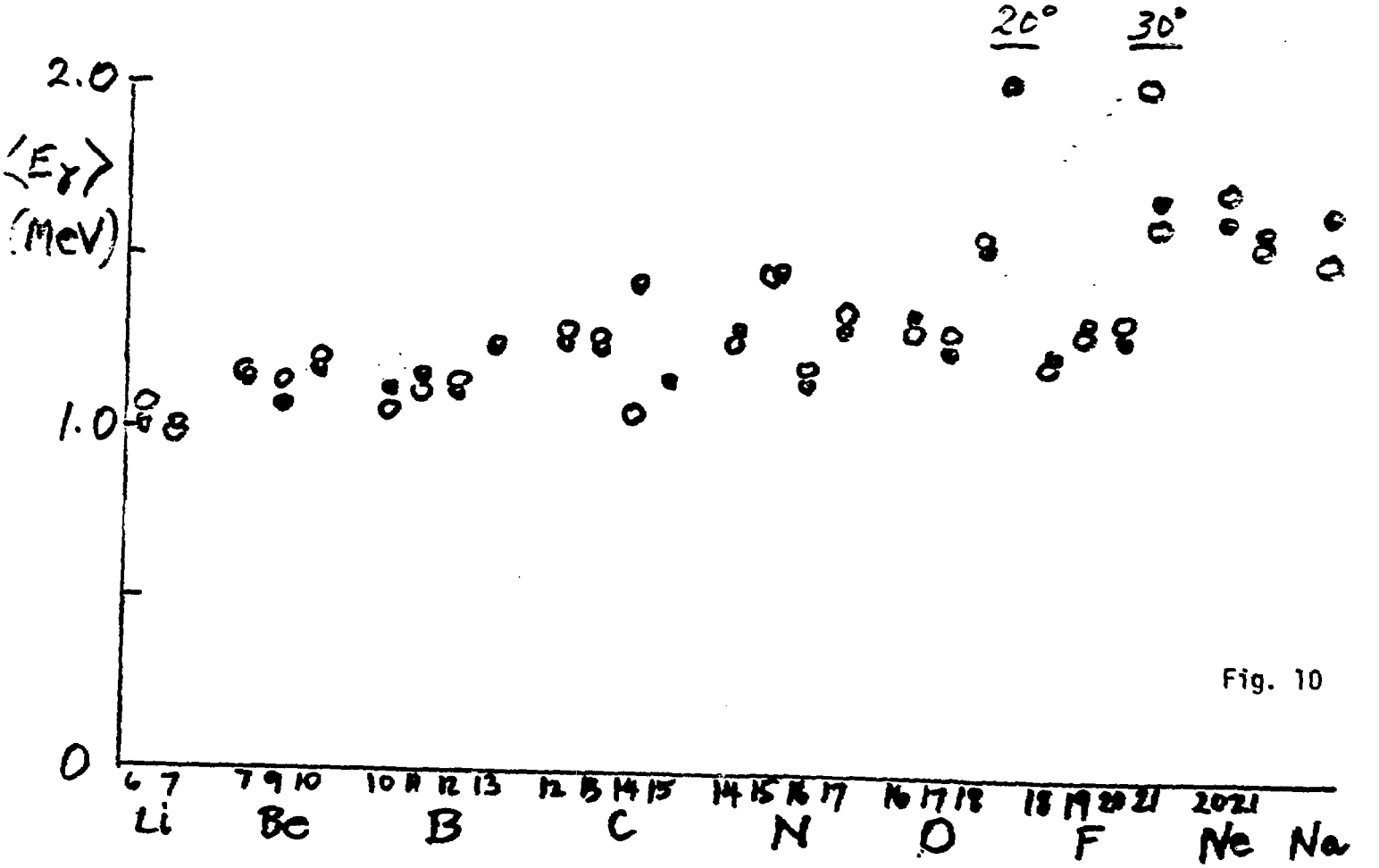
20°
30°
2.0
⟨Eγ⟩
(MeV)
1.0
0
6 7
7 9 10
10 11 12 13
12 13 14 15
14 15 16 17
16 17 18
18 19 20 21
20 21
Li
Be
B
C
N
O
F
Ne
Na

Fig. 10

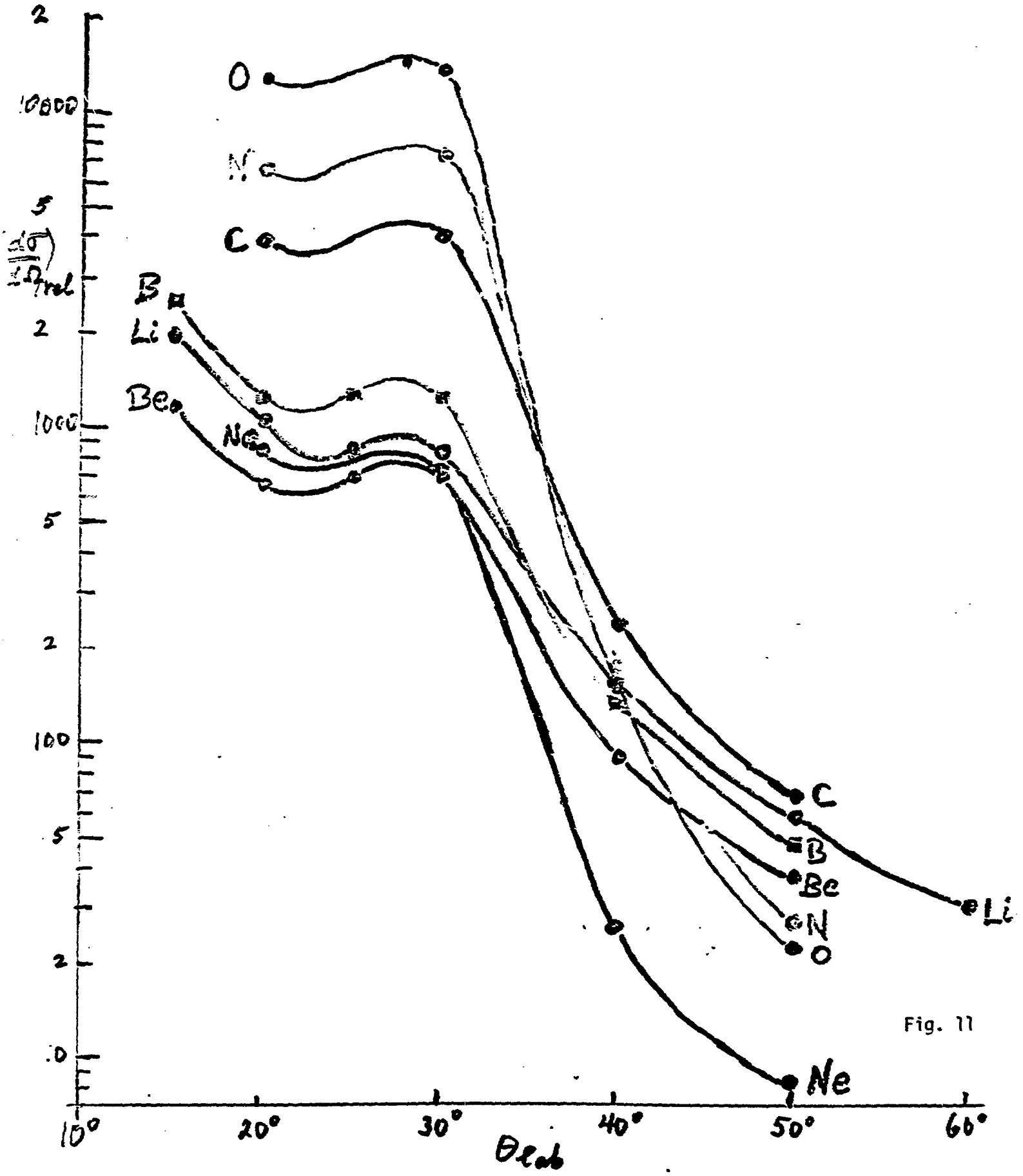
2
10000
5
2
1000
5
2
100
5
2
.0
O
N
C
B
Li
Be
Ne
C
B
Be
N
O
Li
Ne
10°
20°
30°
40°
50°
60°
θlab

Fig. 11

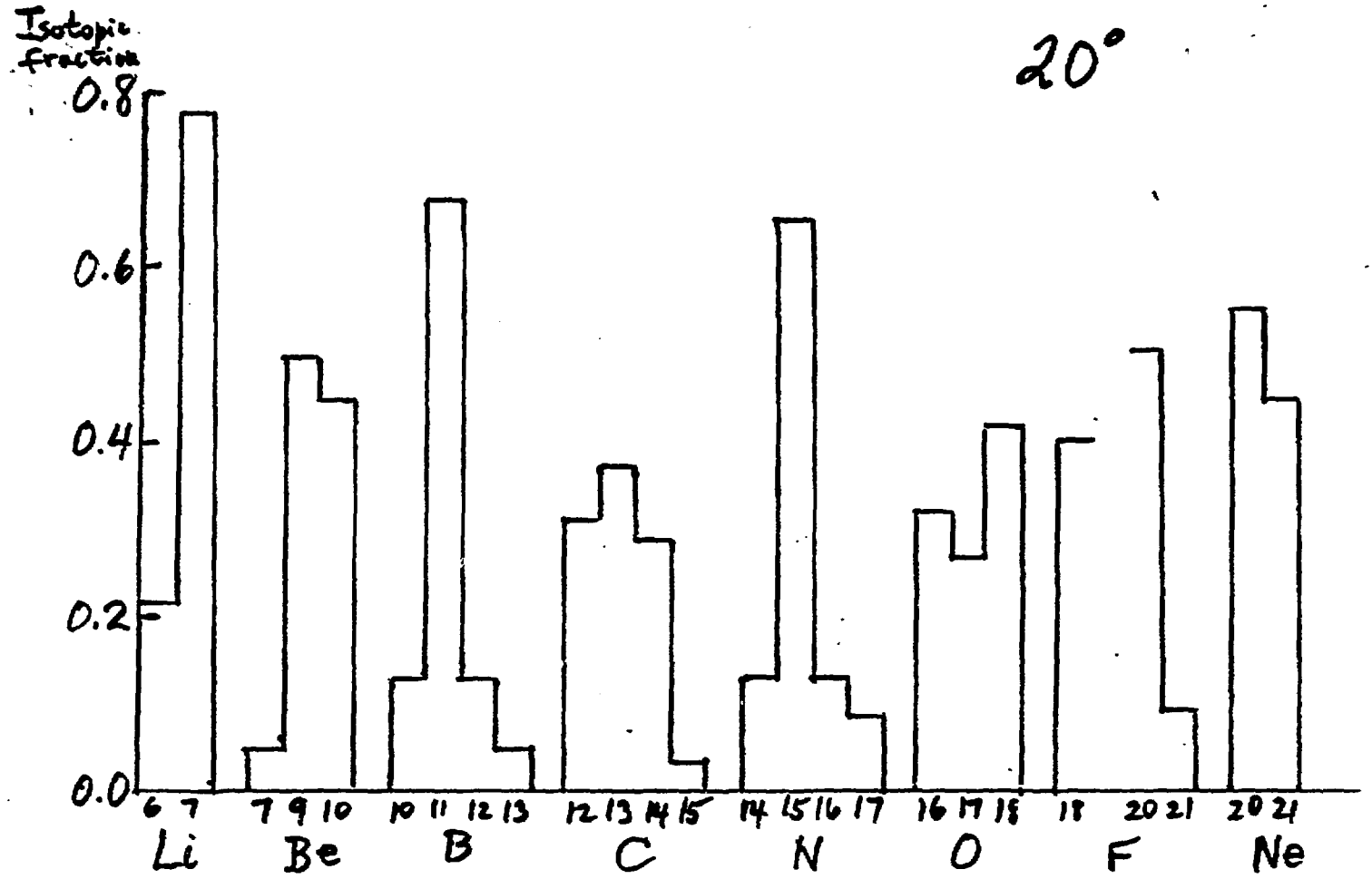
Isotopic fraction
20°
0.8
0.6
0.4
0.2
0.0
6 7
7 9 10
10 11 12 13
12 13 14 15
14 15 16 17
16 17 18
18
20 21
20 21
Li
Be
B
C
N
O
F
Ne

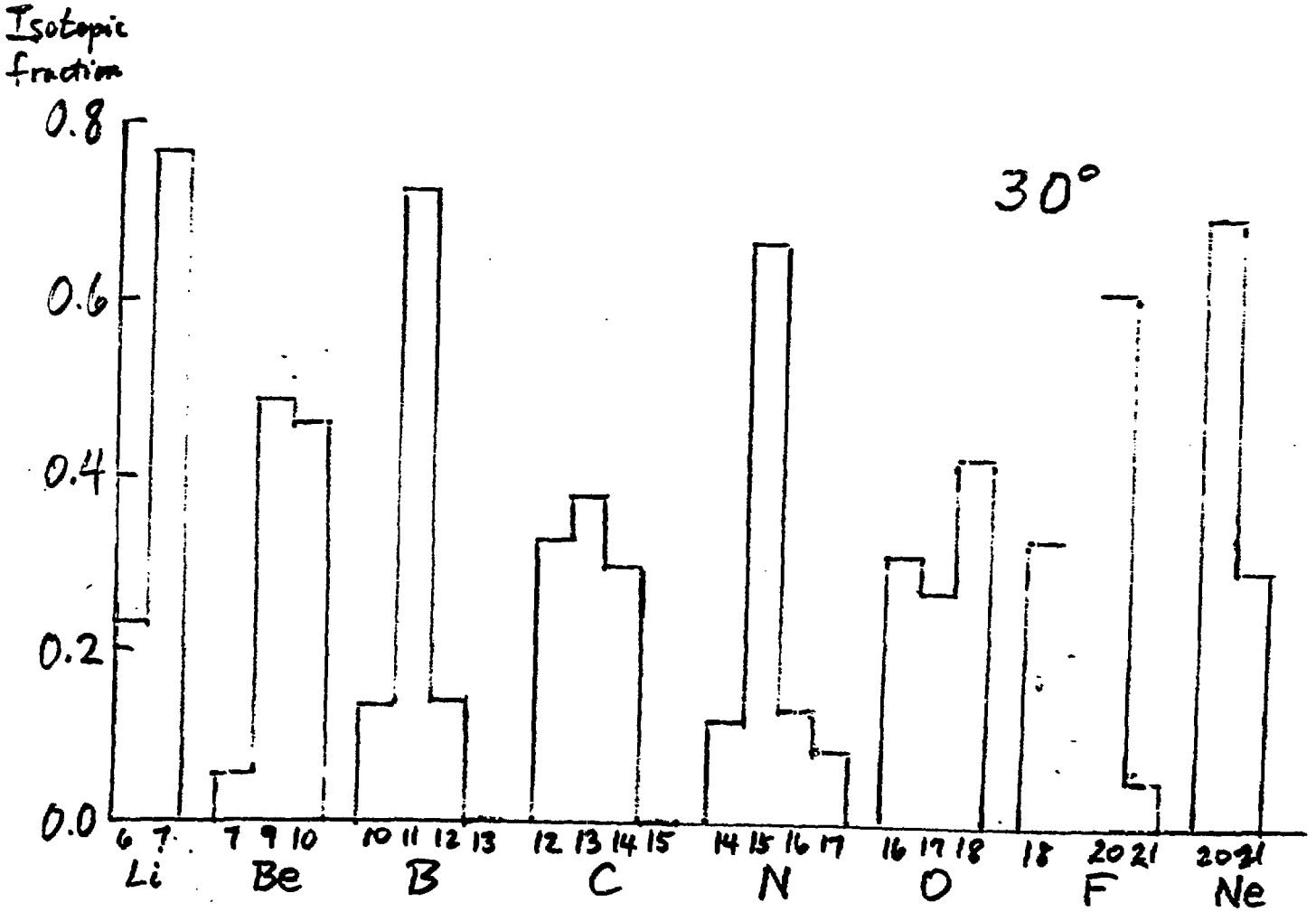
Isotopic fraction
30°
0.8
0.6
0.4
0.2
0.0
6 7
7 9 10
10 11 12 13
12 13 14 15
14 15 16 17
16 17 18
18
20 21
20 21
Li
Be
B
C
N
O
F
Ne

Fig. 12

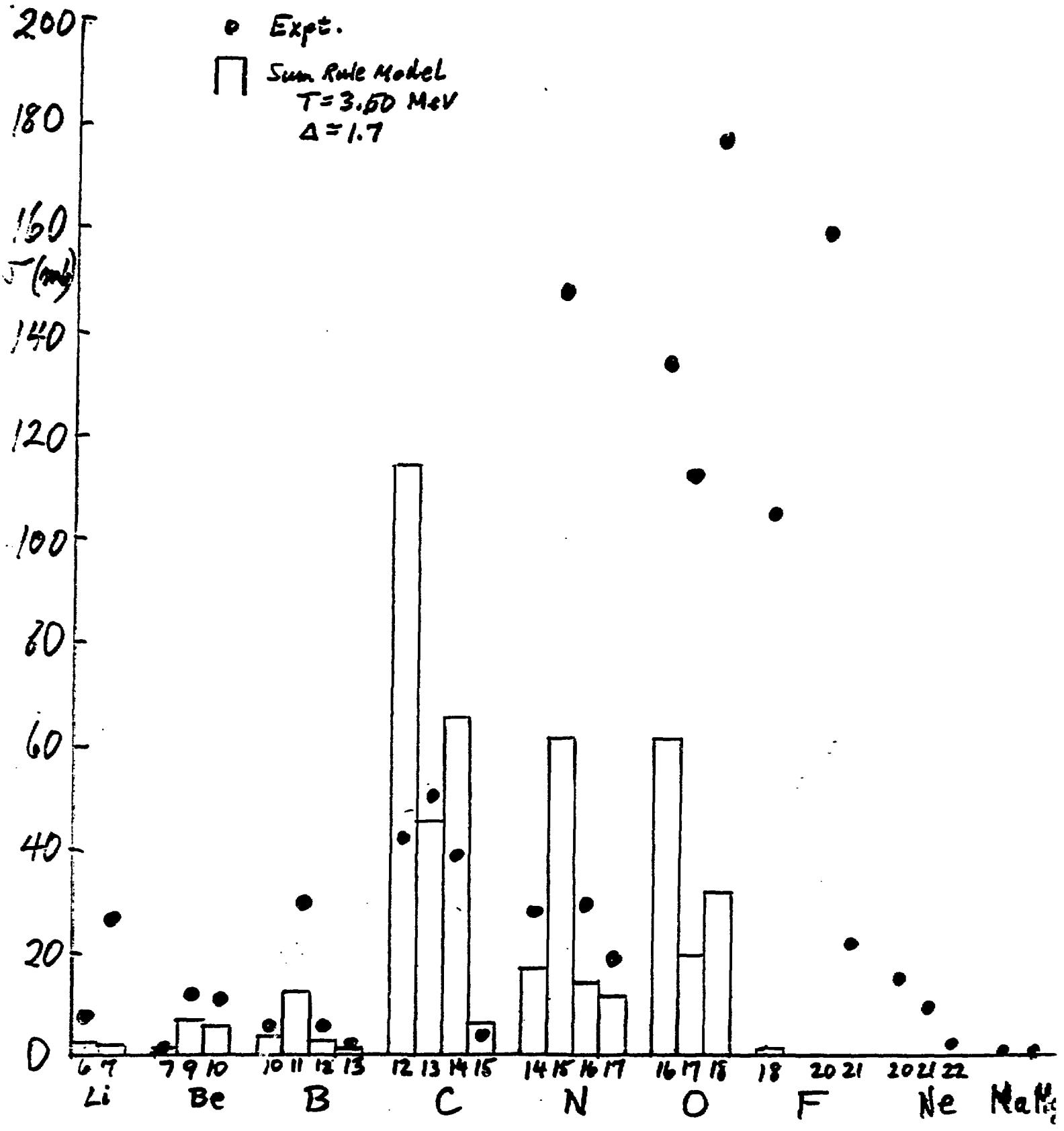
Expt.
Sum Rule Model
T = 3.60 MeV
Δ = 1.7
200
180
160
140
120
100
80
60
40
20
0
6 7
7 9 10
10 11 12 13
12 13 14 15
14 15 16 17
16 17 18
18
20 21
20 21 22
Li
Be
B
C
N
O
F
Ne

Fig. 13

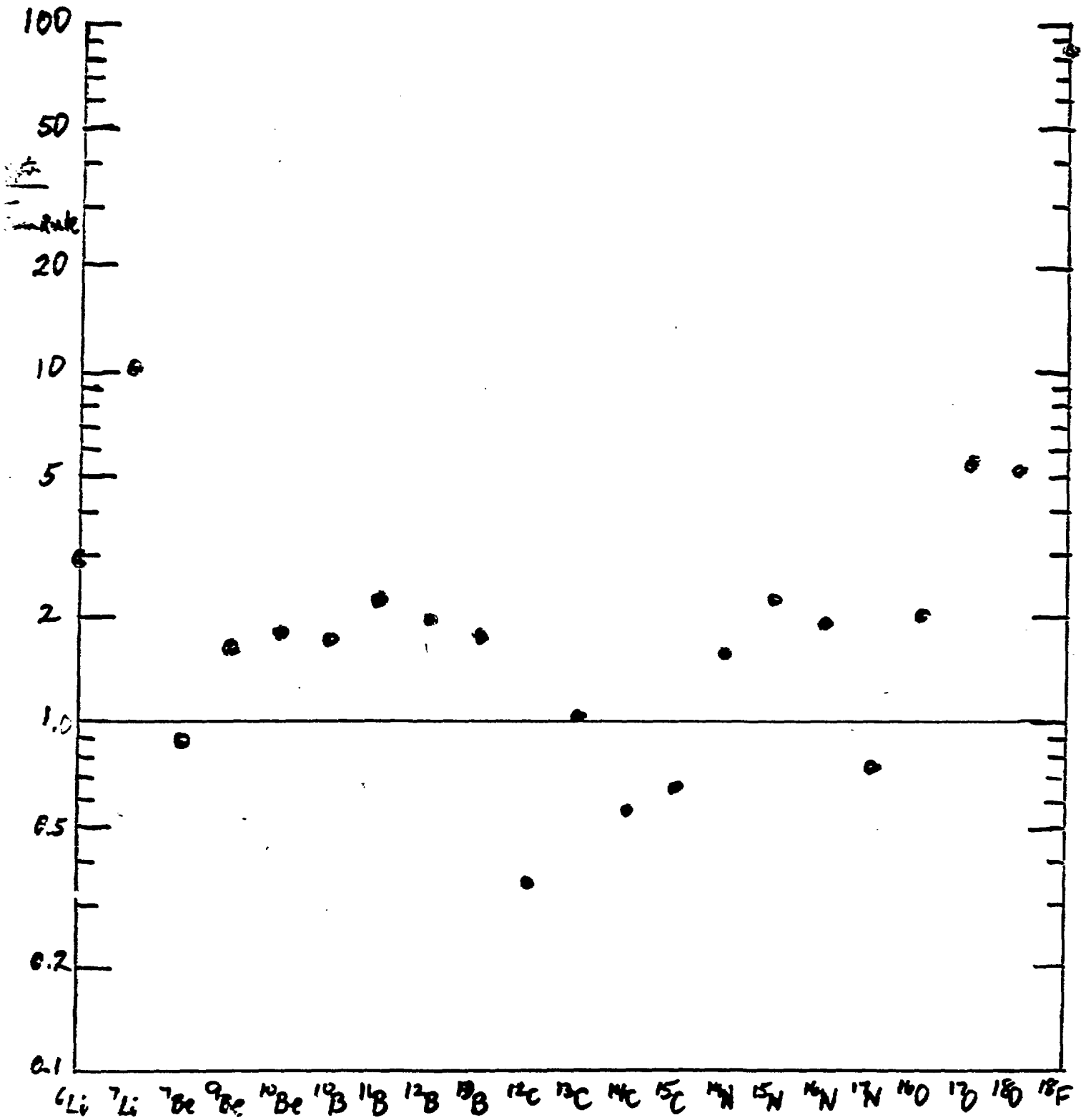
100
50
20
10
5
2
1.0
0.5
0.2
0.1
^{6}Li ^{7}Li ^{7}Be ^{9}Be ^{10}Be ^{10}B ^{11}B ^{12}B ^{13}B ^{12}C ^{13}C ^{14}C ^{15}C ^{14}N ^{15}N ^{16}N ^{17}N ^{16}O ^{17}O ^{18}O ^{18}F

Fig. 14